A Clinically Relevant Approach to Imaging Prostate Cancer: *Review*

Sadhna Verma[1], Arumugam Rajesh[2]

Objective

The purpose of this article is to review the role of MRI in prostate cancer with an emphasis on functional imaging techniques. This article discusses the anatomy of the prostate, the diagnosis of prostate cancer, and the role of different MR techniques in the detection and management of prostate cancer.

Conclusion

Imaging provides important information for the diagnosis and management of prostate cancer.

Introduction

The incidence and mortality of prostate cancer vary substantially worldwide, but it is the most common noncutaneous malignancy in the western world. Prostate cancer is the most common cancer and the second most common cause of cancer deaths among men in the United Kingdom and United States [1]. The death rates from prostate cancer have been declining since the mid 1990s, and these declines may be attributed to earlier diagnosis and treatment. The 5-year survival is effectively 100% when the disease is local or regional but drops to 34% with distant metastases. For all stages, survival is 99% at 5 years, 92% at 10 years, and 61% at 15 years. The management of prostate cancer is a complex issue because of the difficulty in accurate staging and in predicting the speed of disease progression [2]. There are multiple options for treatment including watchful waiting, hormonal treatment, radical prostatectomy (open, laparoscopic, or robotic), various forms of radiation therapy (conformal or intensity-modulated external beam and permanent interstitial or high-dose-rate brachytherapy), or combined approaches [3, 4].

The current methods of prostate cancer detection include digital rectal examination (DRE), serum prostate-specific antigen (PSA) level, and transrectal ultrasound with sextant biopsy. The Gleason score or various nomograms that incorporate several of these factors, with the Partin Tables being the most widely known, are useful in stratifying patients into different risk groups. The role of MRI has evolved over the past decade with the development of newer techniques to localize, stage, and obtain functional information about the tumor.

Anatomy

Zonal Anatomy

The zonal anatomy of the prostate is likened to a cone containing a scoop of ice cream [5, 6]. The cone is the peripheral zone and makes up 70% of the prostate gland by volume in young men. The ducts of the peripheral zone glands drain to the distal prostatic urethra. The scoop of ice cream is the central zone and makes up 25% of the prostate gland volume in young men. The ejaculatory ducts traverse the central zone, and the ducts of the central zone drain to the region of the verumontanum clustered around the entry of the ejaculatory ducts. The remaining 5% of the prostate consists of the transition zone, which is composed of two small bulges of tissue that surround the anterior and lateral parts of the proximal urethra in a horseshoelike fashion (Fig. 1). This two-compartment model is deficient anteriorly where the peripheral zone is interrupted by the anterior fibromuscular stroma, a band of smooth muscle mixed with fibrous tissue that forms a thick shield over the anterior aspect of the gland. As a result, the peripheral zone lies predominantly lateral and posterior to the central zone.

The prostate zones are defined histologically and therefore many prostatic diseases have a zonal distribution. Seventy percent of adenocarcinomas arise in the peripheral zone and 20% of adenocarcinomas arise in the transition zone, while only 10% of adenocarcinomas arise in the central zone. Prostate adenocarcinomas arise in the glandular components of the prostate [5].

Neurovascular Bundle

Sympathetic nerve fibers from the lumbar sympathetic chain pass inferiorly into the pelvis alongside the aorta and iliac arteries. Parasympathetic fibers enter the pelvis as direct branches of S2 to S4. Both sets of fibers intermix as a mesh of nerves posterior to the bladder, seminal vesicles, and prostate. This mesh is known as the "pelvic plexus."

Keywords: diffusion-weighted imaging, dynamic contrast enhancement, prostate cancer, prostate cancer imaging, prostate MRI, prostate MR spectroscopy

DOI:10.2214/AJR.09.7196

Received August 11, 2009; accepted after revision December 28, 2009.

[1]Department of Radiology, Section of Abdominal Imaging, University of Cincinnati Medical Center, 234 Goodman St, Cincinnati, OH 45219. Address correspondence to S. Verma (drsadhnaverma@gmail.com).

[2]Department of Radiology, University Hospitals of Leicester NHS Trust, Leicester General Hospital, Leicester, United Kingdom.

AJR 2011; 196:S1–S10 0361–803X/11/1963–S1

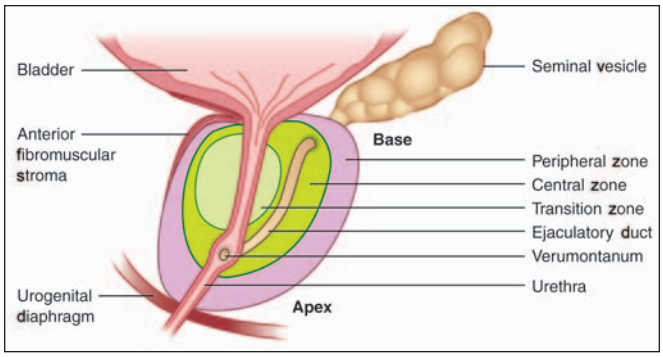

Fig. 1—Schematic shown in sagittal view of prostate illustrates normal zonal description of prostatic anatomy.

The cavernous nerve arises as many fine fibers from the pelvic plexus, containing both sympathetic and parasympathetic nerves. The cavernous nerve then runs inferiorly, as one of several large bundles, along the posterolateral aspect of the prostate. Arterial and venous prostatic vessels in this location accompany the cavernous nerve, and together these structures form the neurovascular bundles.

Prostatic Anatomy as Seen on MRI

The zonal anatomy of the prostate cannot be distinguished on T1-weighted images because the prostate appears to be of uniform intermediate signal intensity. However, the prostatic zones are well shown on T2-weighted

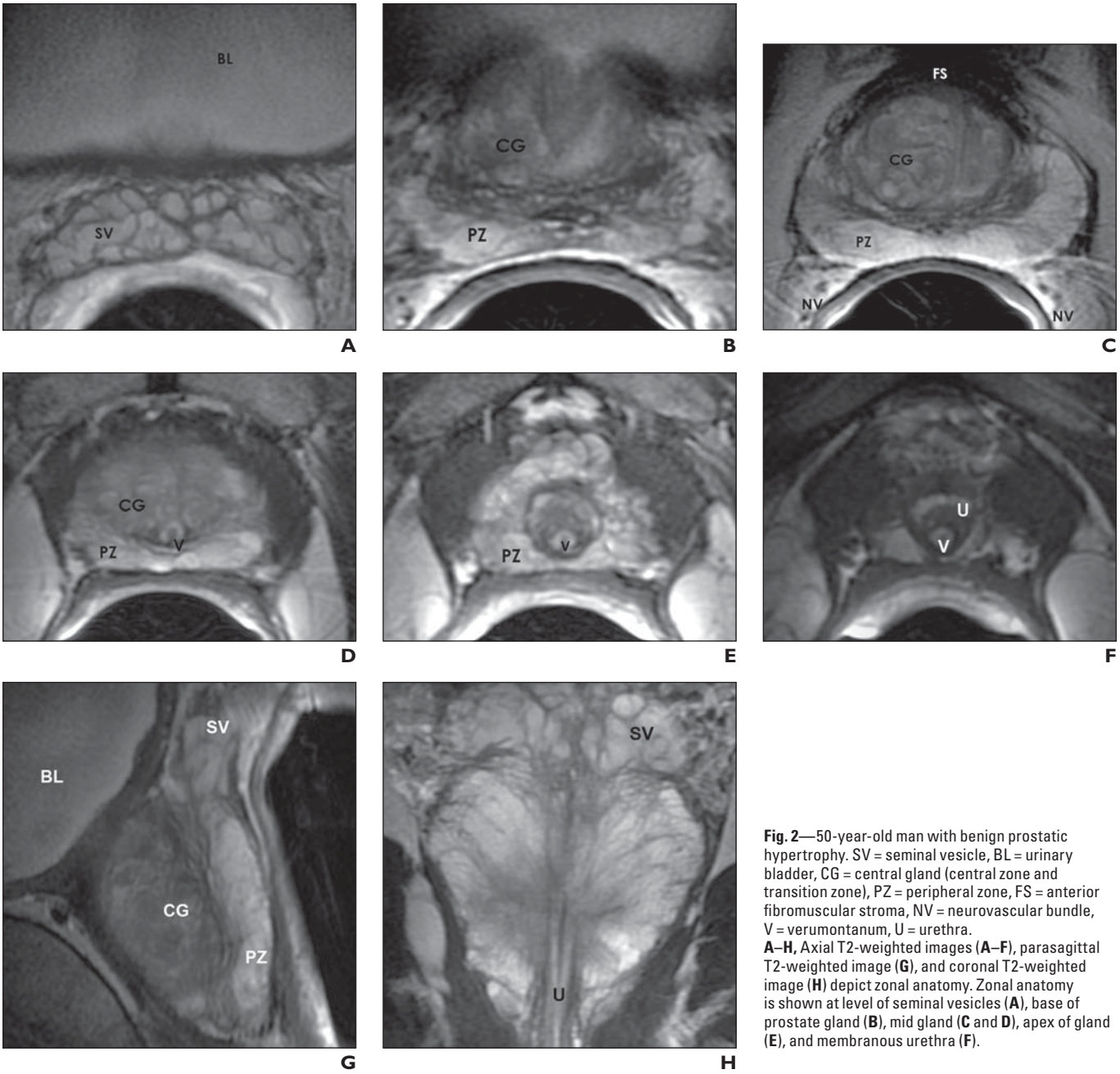

Fig. 2—50-year-old man with benign prostatic hypertrophy. SV = seminal vesicle, BL = urinary bladder, CG = central gland (central zone and transition zone), PZ = peripheral zone, FS = anterior fibromuscular stroma, NV = neurovascular bundle, V = verumontanum, U = urethra.
A–H, Axial T2-weighted images (**A–F**), parasagittal T2-weighted image (**G**), and coronal T2-weighted image (**H**) depict zonal anatomy. Zonal anatomy is shown at level of seminal vesicles (**A**), base of prostate gland (**B**), mid gland (**C** and **D**), apex of gland (**E**), and membranous urethra (**F**).

images (Fig. 2). The anterior fibromuscular stroma is of low T1 and T2 signal intensity. The peripheral zone has high T2 signal intensity similar to or greater than the signal of adjacent periprostatic fat. The anatomic or true capsule surrounding the peripheral zone appears as a thin rim of low signal intensity on T2-weighted images [5, 6]. The central and transition zones are both of lower T2 signal intensity than the peripheral zone, possibly because of more compact smooth muscle and sparser glandular elements. There is also an age-related increase in the T2 signal intensity of the peripheral zone [7].

The prostate gland is partially invested by a coalition of fibrous tissue—historically, called the "capsule"—that is most apparent posteriorly and posterolaterally. The capsule is an important landmark for assessing extraprostatic tumor extension. The neurovascular bundles course posterolateral to the prostate capsule bilaterally at the 5- and 7-o'clock positions (Fig. 2C). At the apex and the base, the bundles send penetrating branches through the capsule, providing a route for extraprostatic tumor extension.

The proximal urethra is rarely identifiable unless a Foley catheter is present or a transurethral resection has been performed. The verumontanum can be visualized as a high-T2-signal-intensity structure. The distal prostatic urethra can be seen as a low-T2-signal-intensity ring in the lower prostate because it is enclosed by an additional layer of muscle (Figs. 2D–2H). The vas deferens and seminal vesicles are particularly well seen on axial and coronal images, and the neurovascular bundles can be seen best on axial images.

The prostate is conventionally described in terms of sextants based on division of the gland into thirds in the craniocaudal direction (base, mid gland, and apex) and then into left and right sides. Accordingly, the six sextants are the left base, left mid gland, left apex, right base, right mid gland, and right apex.

Diagnosis

Prostate carcinoma is often diagnosed when the serum PSA value is elevated or when DRE findings are abnormal. A serum PSA level of greater than 4 ng/mL is considered abnormal. However, it is also well recognized that nearly one third of biopsy-proven prostate cancers present with normal PSA levels and that 70–80% of patients with elevated PSA levels (> 4 ng/mL) do not have prostate carcinoma [8, 9]. DRE is not accurate for staging. Tests based on PSA—that is, PSA derivatives, which are namely PSA density, PSA velocity, age-specific reference range, PSA isoforms, and percentage of free PSA—are being developed to improve on traditional serum PSA testing [10].

Transrectal ultrasound–guided biopsy is the universally accepted method of confirming the presence of prostate cancer. A sextant approach is used to obtain the biopsy samples because ultrasound has poor sensitivity for visualizing the tumor. The yield from this approach varies [11, 12].

Three cores of each lobe (i.e., the base, mid gland, and apex) along a parasagittal plane yielded an approximately 25% cancer detection rate when serum PSA level was between 4 and 20 ng/mL [13]. Repeat biopsy showed cancer in approximately 20% of men with a persistently elevated level of serum PSA and a negative initial biopsy [14, 15]. Presti et al. [16] achieved approximately 40% yield using a 10-core approach, and obtaining even more than 10 cores has been advocated to minimize sampling errors.

Ninety-five percent of prostate cancers are adenocarcinomas that develop from the acini of the prostatic ducts. They are classified by Gleason score. Tumors are assigned a primary

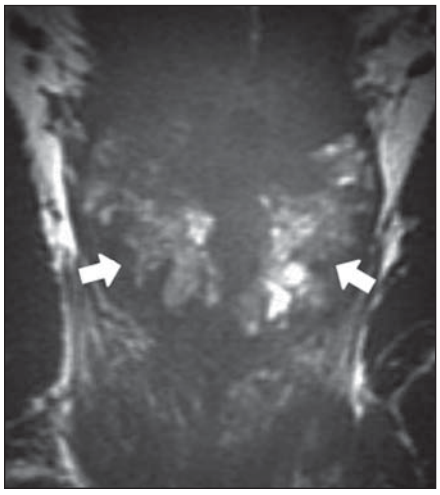

Fig. 3—50-year-old man with prostate cancer who underwent ultrasound-guided prostate biopsy 5 weeks before MRI. Coronal T1-weighted image shows extensive bilateral hemorrhage (*arrows*). Patient was rescheduled for preoperative MRI evaluation.

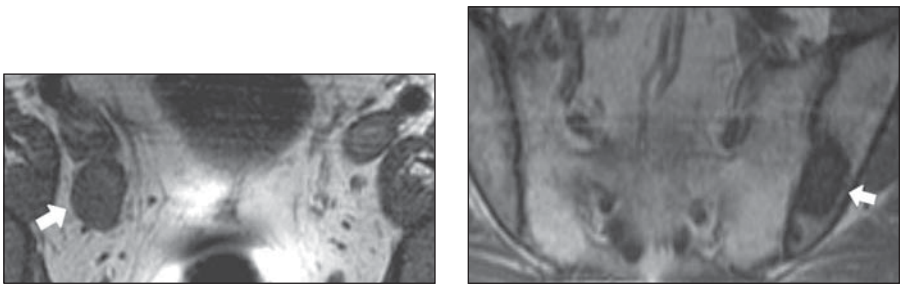

A **B**

Fig. 4—60-year-old man with prostate-specific antigen level of 10.7 ng/mL and biopsy-confirmed Gleason grade 7 (4 + 3) prostate cancer.
A, Axial T1-weighted image shows right iliac lymphadenopathy (*arrow*).
B, Axial T1-weighted image shows left iliac bone metastasis (*arrow*).

TABLE 1: Staging Systems for Prostate Cancer

Jewett-Whitmore	TNM	Description
A	I (T1N0M0)	Organ-confined tumor that is clinically and radiologically inapparent
B	II (T2N0M0)	Organ-confined tumor that is clinically or radiologically apparent: T2A = localized to a quadrant T2B = localized to one side T2C = bilateral
C	III (T3N0M0)	Extracapsular extension or seminal vesicle invasion[a]: T3A = unilateral or bilateral extracapsular extension T3B = seminal vesicle invasion
D1	IV (N1–2)	Locoregional adenopathy: N1 = microscopic nodal metastases N2 = macroscopic nodal metastases
D2	IV (T4 or N3 or M1–2)	Distant spread: T4 = invasion of the bladder, external sphincter, or rectum N3 = extraregional nodal metastases M1 = elevated acid phosphatase M2 = distant visceral or bony metastases

[a]In the fourth edition of the American Joint Committee on Cancer staging system, unilateral and bilateral extracapsular extension were classified separately as T3A and T3B, respectively. This distinction was dropped from the fifth and subsequent editions.

grade on the basis of the predominant pattern of differentiation and a secondary grade on the basis of the second most common pattern. The primary grade, which describes the predominant pattern of differentiation, determines the aggressiveness of the tumor [17, 18].

Well-differentiated cancers have a Gleason score lower than 6 and are associated with a good prognosis. Those with a Gleason score of 8–10 have the worst prognosis and the highest risk for recurrence. Tumors with Gleason scores of 7 have a variable prognosis and intermediate risk of recurrence.

The use of nomograms (e.g., D'Amico, Partin, or Kattan) can significantly improve accuracy in predicting the risk of treatment failure compared with a single parameter alone [18, 19]. These nomograms provide general probabilities and not the specific risk for an individual patient. Recently, the number of positive biopsy cores, the amount of cancer in each core, and the location of large-volume cores have been taken into consideration to improve the accuracy of local staging [20–22]. Imaging can aid in risk stratification and treatment. Endorectal MRI contributes incrementally to the value of staging nomograms in predicting organ-confined prostate cancer [23–25].

Staging

The TNM and Jewett-Whitmore staging systems are in common usage and are based on the local, nodal, and distant extent of disease [26]. A summary of the staging systems is given in Table 1. Staging of prostate cancer is central to management because it contributes both to predicting prognosis and planning treatment. Despite the prevalence of prostate cancer, published studies on prognosis are relatively sparse. Good prognostic studies are lacking because the mortality from unrelated causes is high in elderly men with prostate cancer.

MRI Techniques in Prostate Cancer

Conventional MRI—The current clinical standard is to perform prostate MRI using endorectal and pelvic phased-array coils on a magnet that is at least 1.5 T. With the use of endorectal coils, high-resolution images, which are necessary

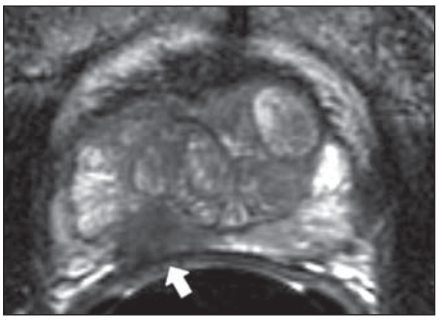

Fig. 5—72-year-old man with biopsy-confirmed Gleason grade 6 (3 + 3) prostate cancer. Axial T2-weighted image shows medial rectoprostatic angle effacement caused by peripheral zone tumor (*arrow*).

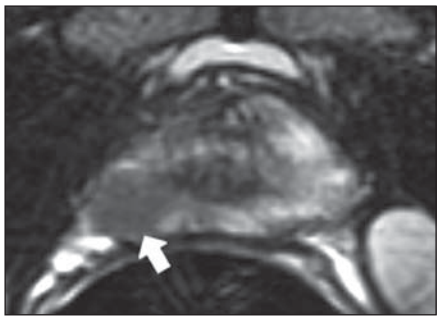

Fig. 6—Prostate cancer in 65-year-old man with Gleason grade of 7 (3 + 4). Axial T2-weighted image shows lateral rectoprostatic angle effacement (*arrow*) caused by peripheral zone tumor.

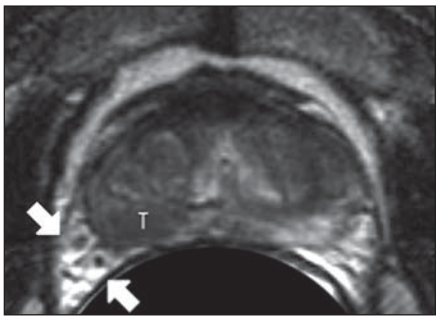

Fig. 7—46-year-old man with biopsy-confirmed Gleason grade 7 (4 + 3) prostate cancer. Axial T2-weighted image shows prostate capsule bulge with asymmetry of neurovascular bundle (*arrows*) on right caused by peripheral zone tumor (T).

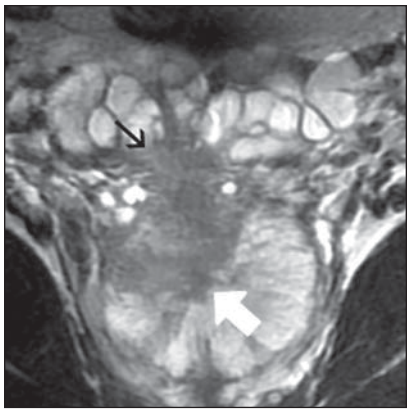

Fig. 8—Prostate cancer in 50-year-old man with Gleason grade of 8 (4 + 4). Coronal T2-weighted image shows ill-defined, 3-cm low-signal mass (*white arrow*) at right base to midgland peripheral zone and central gland with extension to right seminal vesicle (*black arrow*).

Fig. 9—63-year-old man who had undergone prostatectomy 10 years earlier for adenocarcinoma presented for follow-up imaging with rising prostate-specific antigen level. Axial T2-weighted fat-suppressed image shows 2-cm soft-tissue mass (*arrow*) inferior to left bladder base and anterior to rectum. No endorectal coil was used because of history of rectal fistula. Targeted biopsy proved recurrent prostate adenocarcinoma.

for accurate localization and staging of prostate cancer, can be obtained [27, 28].

Although MRI is the most sensitive imaging technique in relation to other imaging techniques for prostate cancer staging at this time, MRI is not widely used because of its low specificity. Prostate adenocarcinoma in the peripheral zone shows low signal intensity that is easily distinguished from the normal high-signal peripheral zone. However, low signal intensity in the peripheral zone is nonspecific and may be seen in benign conditions such as biopsy-related hemorrhage, changes from hormone therapy, prostatitis, and postradiation fibrosis. Therefore, conventional MRI evaluation of prostate cancer is usually combined with one or more of several functional techniques such as MR spectroscopy (MRS), diffusion-weighted imaging (DWI), and dynamic contrast-enhanced MRI (DCE-MRI). Each of the functional MR techniques has clinical advantages and limitations. The optimal combination of anatomic and functional MR sequences still needs to be established.

Conventional MRI evaluation for the assessment of cancer usually involves a combination of anatomic T1- and T2-weighted images. At our institution, prostate MRI is performed with both 1.5- and 3-T magnets using an endorectal coil and a commercially available 8-channel body-array coil. The endorectal coil is inserted and inflated with approximately 60–80 mL of liquid perfluorocarbon.

T1-weighted images are acquired from the aortic bifurcation to the pelvis to check for postbiopsy hemorrhage (Fig. 3) within the prostate or seminal vesicles and for metastases to the pelvic bone and lymph nodes (Figs. 4A and 4B). Postbiopsy hemorrhage can distort image quality as well as mask tumor; therefore, an 8- to 10-week wait between prostate biopsy and MRI examination is recommended [29].

Multiplanar high-resolution fast spin-echo (FSE) T2-weighted images of the prostate are acquired to detect and localize prostate cancer [30]. Multiplanar T2-weighted images of the entire prostate can be obtained in three planes (axial, coronal, and sagittal) at a resolution of 0.7 × 0.5 mm (field of view, 140 mm; matrix, 256 × 192; TR/TE, 6000/102; slice thickness, 3 mm) on a 1.5-T magnet. The presence of extraprostatic extension can also be seen on axial T2-weighted images (Figs. 5–7). The signs of extracapsular extension are summarized in Table 2. Tumor is seen as low signal intensity in the high-signal peripheral zone. Seminal vesicle invasion can also be depicted well on T2-weighted images (Fig. 8). Normal seminal vesicle has high signal intensity (Fig. 2H). MRI can also be used to detect recurrent disease in patients who have undergone prostatectomy (Fig. 9).

MR Spectroscopy

Spectroscopy assesses the relative concentration of different chemical compounds in tissue. Currently, proton (hydrogen) MRS is commercially available for the prostate using a 3D chemical-shift imaging technique [31]. Prostate MRS has been performed predominantly using a multivoxel technique, with which intracellular metabolic information can be obtained from single or multiple sections. This technique provides information about the spatial distribution of metabolites and is useful for studying multiple lesions.

On MR spectroscopy, the resonances for the prostate metabolites—choline, creatine, polyamines, and citrate—occur at distinct frequencies (≈ 3.2, 3.0, 3.1, and 2.6 ppm, respectively) or positions in the spectrum; when MRS is performed at 1.5 T, the peaks for choline, creatine, and polyamines overlap. The areas under these signals are related to the concentration of the respective metabolites, and changes in these concentrations can be used to identify cancer.

The healthy prostate gland produces a high level of citrate and normally has high levels of polyamines. In prostate cancer, citrate and polyamine levels decrease markedly [32]. Prostate cancer also leads to increased choline because

TABLE 2: Signs of Extracapsular Extension

Asymmetric prostate capsular bulge with irregular margins
Obliteration of the rectoprostatic angle
Asymmetry of neurovascular bundle
Tumor encasement of the neurovascular bundle
Seminal vesicle invasion

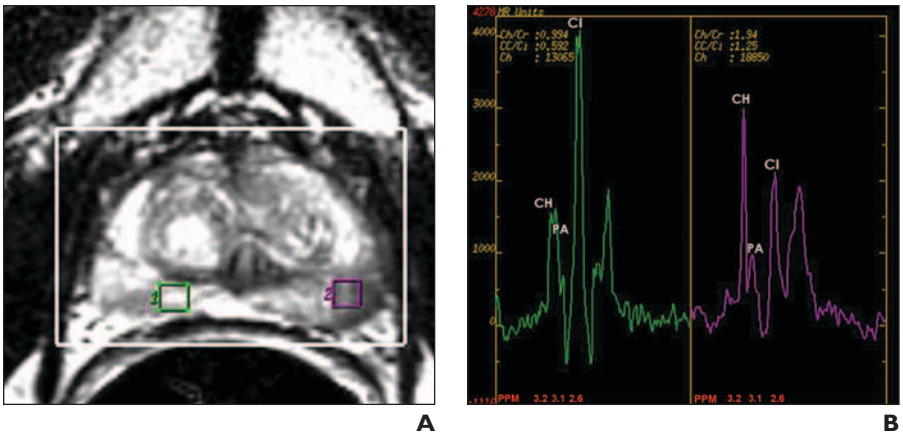

A B

Fig. 10—Prostate cancer in 45-year-old man with Gleason grade of 6 (3 + 3).
A, Axial T2-weighted image with voxel on normal prostatic tissue (*green*) and cancer (*purple*).
B, Normal (*green*) and abnormal (*purple*) MR spectra corresponding to regions of interest in **A** show elevated choline and creatine (Ch + Cr) to citrate (Ci) ratio. CI = citrate, CH = choline, PA = polyamine.

of higher cell membrane turnover, cell density, and phospholipid metabolism. The ratio of choline to citrate is increased in cancer (Figs. 10A and 10B). Because the resonant peak of creatine is close to that of choline, the ratio of choline plus creatine (Ch + Cr) to citrate (Ci) is typically measured on clinical spectroscopy [32].

Three-dimensional MRS data are acquired using a water- and lipid-suppressed double spin-echo point-resolved spectroscopy (PRESS) sequence [33]. Water and lipid suppression is achieved using either band-selective inversion with gradient dephasing (BASING) pulses placed in the PRESS volume selection [33, 34] or using spectral-spatial pulses capable of both volume selection and frequency selection [35, 36]. A number of additional steps need to be taken to ensure good water and lipid suppression. First, the axial T2-weighted images typically are used to graphically select the PRESS volume with the goal of maximizing coverage of the prostate while minimizing the inclusion of periprostatic fat and rectal air. The volume is often oblique in the *z*-axis because the long axis of the prostate is usually angled anteriorly (typically from 0° to 25°) in this direction. Second, the pulses used for volume selection must be very selective because many important prostate cancers occur at the periphery of the gland at the prostate-rectum and periprostatic lipid interface. Third, the sharpness of the PRESS volume selection is enhanced through the use of the Shinnar-Le Roux 90° and 180° pulses or through the use of high-bandwidth spectral-spatial 180° pulses that also reduce chemical-shift misregistration errors [35, 36].

Even with the use of these optimized pulses, spectroscopic voxels at the edge of the PRESS volume can still be contaminated by residual signal arising in adjacent tissues. To further reduce contamination from the tissues surrounding the prostate, the selected volume is automatically overprescribed by 30% and recently developed, very selective, outer-volume saturation pulses with very sharp transition bands are placed at the edges of the originally selected volume. The spectroscopist graphically places additional very selective, outer-volume saturation pulses to better conform the rectangular PRESS volume to the shape of the prostate. This often involves placing saturation bands across the corners of the PRESS volume to eliminate periprostatic lipids that normally occupy these regions.

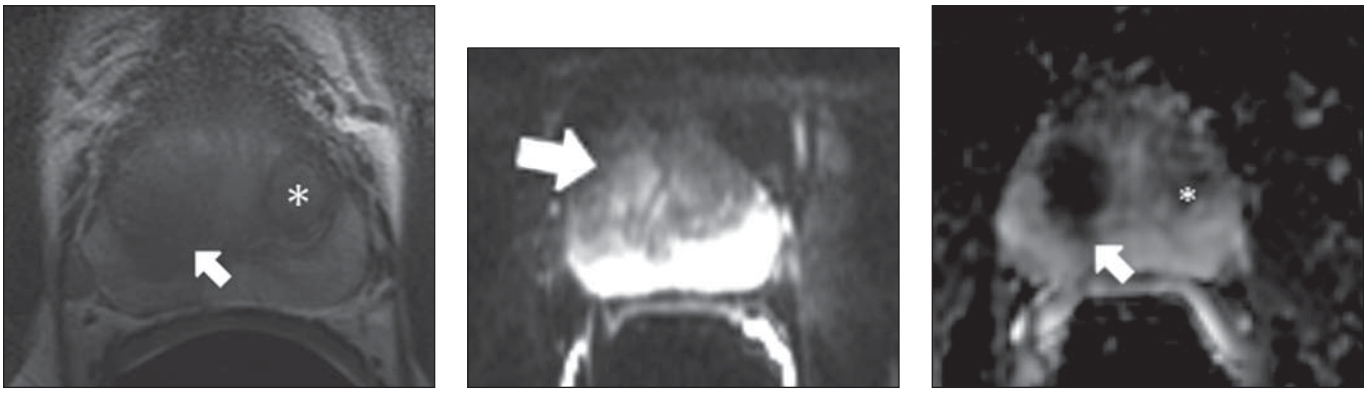

A B C

Fig. 11—54-year-old man with Gleason grade 7 (3 + 4) biopsy-proven prostate cancer.
A, Axial T2-weighted image shows ill-defined low-signal mass in right mid gland (*arrow*) and well-defined low-signal focus in left mid gland (*asterisk*) on T2-weighted image.
B, Raw diffusion-weighted image shows high signal intensity in right midgland prostatic tumor due to restricted diffusion (*arrow*). Note focus in left mid gland is homogeneous with remainder of central gland.
C, Apparent diffusion coefficient (ADC) map derived from diffusion-weighted images shows low ADC value in right midgland lesion (*arrow*); this finding is indicative of restricted diffusion in tumor. Well-defined focus in left mid gland corresponds to region of stromal benign prostatic hyperplasia as shown by striated signal loss (*asterisk*). Targeted biopsy confirmed these findings.

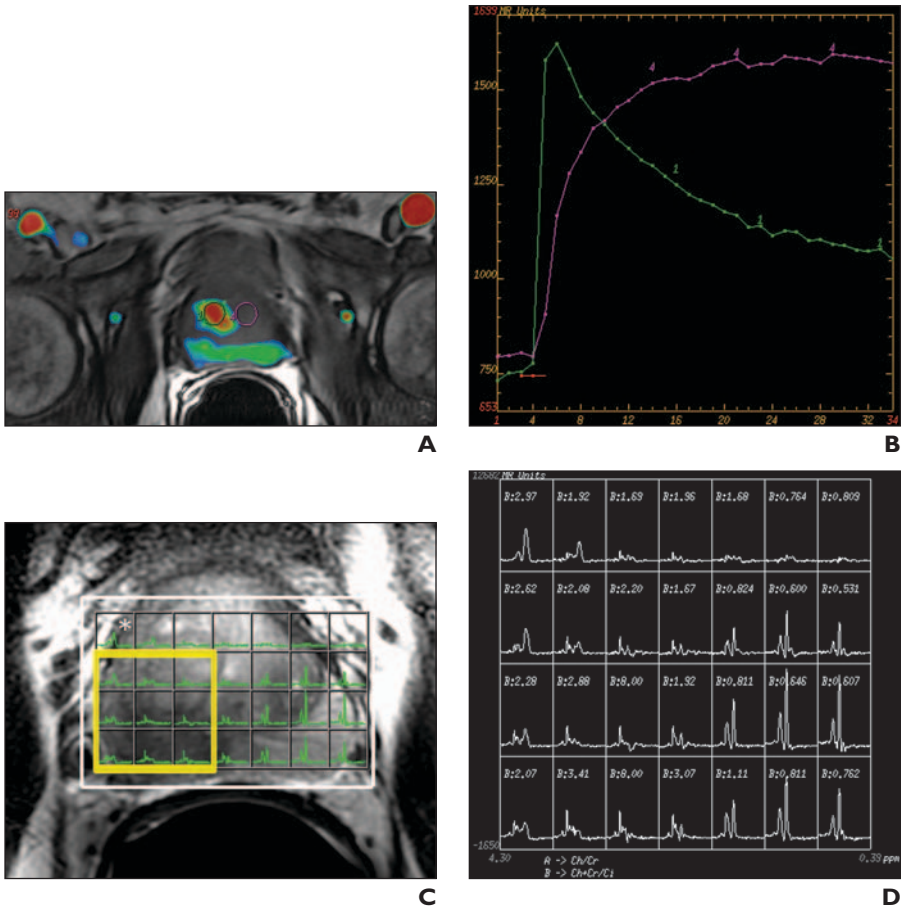

Fig. 12—52-year-old man with biopsy-proven adenocarcinoma of Gleason grade 7 (4 + 3). Perfusion images were acquired using fast-field echo sequence (TR/TE, 17/2.9; flip angle, 15°) and MR spectroscopy was also performed.
A, Axial contrast-enhanced image shows region-of-interest (ROI) cursors. Region of abnormal enhancement is shown in red.
B, Time–signal intensity curves (*x*-axis = time; *y*-axis = MR signal) for ROIs show abnormal enhancement pattern for ROI 1 and normal enhancement pattern for ROI 4. Note that there is high relative peak enhancement and fast wash-in and washout in region of tumor.
C, Axial T2-weighted image with overlying spectroscopy grid shows abnormal spectra in yellow box. Note that region of asterisk partially lies outside prostate gland, so it cannot be included in evaluation.
D, MR spectra obtained using 3-T unit show high choline and creatine (Ch + Cr) to citrate (Ci) ratio at right base and mid gland; this finding is indicative of tumor and was confirmed at biopsy.

Datasets are typically acquired as 16 × 8 × 8 phase-encoded spectral arrays (1024 voxels) with a nominal spectral resolution of 0.24–0.34 cm^3, TR/TE of 1000/130, and 17-minute acquisition time on a 1.5-T scanner. In current commercially available prostate MRI and MRS units, the MRS data can be processed and displayed on the MR scanner just like MR images. The display of MR images and MRS images typically involves overlaying the spectroscopic grid on the T2-weighted image and plotting the corresponding spectroscopic array.

A standardized scoring system for MRS of the prostate has been developed to assess MR spectra in the peripheral zone that is based primarily on the choline plus creatine (Ch + Cr) to citrate (Ci) ratio and secondarily on spectral-signal-to-noise and choline-to-creatine ratios as well as polyamine levels [37]. The scoring system assigns spectral voxels a score from 1 to 5 on the basis of these ratios and levels, with a score of 4 or 5 indicating an area of likely malignancy. The scoring system has shown specificities of 84.6% and 89.3% and sensitivity from 64% to 93% when a voxel score of 4 or 5 was used to identify cancer [37]. MRS is performed after the conventional MR examination so that the spectral information can be overlaid directly on the T2-weighted images to localize abnormalities.

Several single-site studies have shown improved detection, localization, and estimation of the aggressiveness of prostate cancer when prostate MRI is used in conjunction with MRS [32, 38]. In addition, MRS has been shown to predict tumor volume, extracapsular extension, radiotherapy response, and recurrence after radiotherapy [32, 39–41]. However, a recent multisite trial led by the American College of Radiology Imaging Network showed no incremental benefit of MRS with MRI in comparison with MRI alone for sextant localization of peripheral zone prostate cancer [42].

The current clinical indications for MRS in prostate cancer are staging, rising PSA level and negative biopsy work-up, guidance for radiation, as well as following patients on active surveillance.

MRS is technically challenging and some of its limitations include a long acquisition time, artifacts from postbiopsy hemorrhage, and difficulty in obtaining optimal shimming and adequate fat and water suppression. Furthermore, to optimize postprocessing of spectroscopic data, manual case-specific adjustments are necessary that often cannot be performed by the commercially available spectroscopy packages and require adequate training.

Diffusion-Weighted Imaging

DWI is used as an adjunct to improve detection and localization of prostate cancer. It is based on the principle of random molecular motion of water in tissues [43]. Healthy

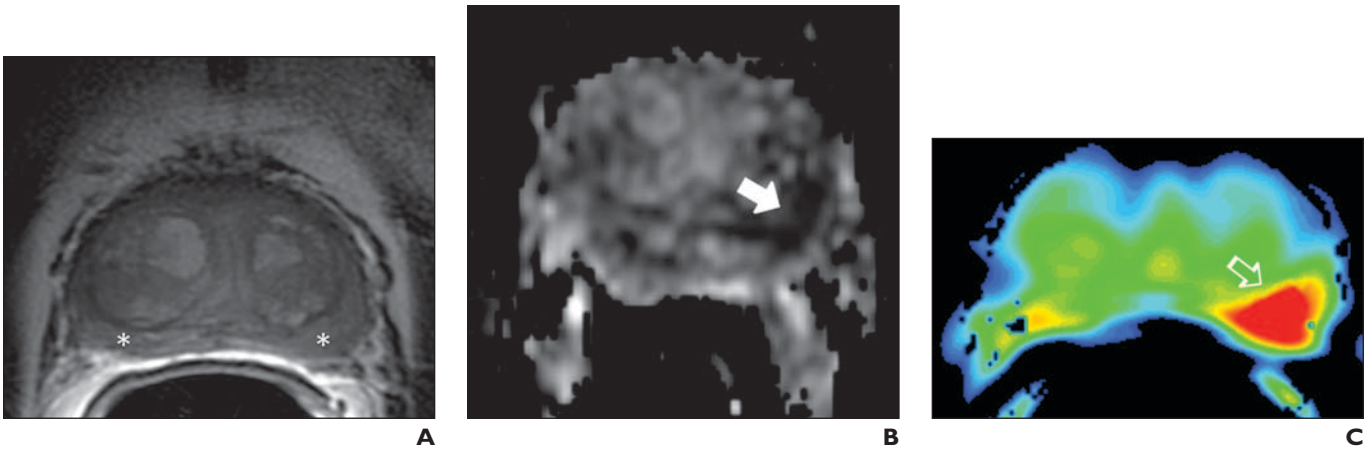

Fig. 13—Biopsy-proven prostate adenocarcinoma in 62-year-old man with Gleason grade of 6 (3 + 3). This example shows how functional imaging can help identify tumor because morphologic T2-weighted images can be nonspecific.
A, Axial T2-weighted image at level of mid gland shows nonspecific low signal bilaterally in peripheral zone (*asterisks*) with minimal capsular bulge on left.
B, Diffusion-weighted image with apparent diffusion coefficient (ADC) map shows low ADC value in left midgland peripheral zone lesion (*arrow*). This finding is indicative of decreased diffusion.
C, Dynamic contrast-enhanced image shows focal area of abnormal enhancement in left mid gland (*arrow*). This area corresponds to region of tumor confirmed at prostatectomy.

prostate tissue exhibits signal loss, whereas areas of restricted molecular motion, such as in densely packed tumor cells, show less signal loss and are therefore bright on the raw DWI. With enhanced gradients, DWI is rapidly becoming useful for prostate imaging. DWI provides both qualitative information and quantitative information that reflect changes at the cellular level about tumor cellularity and cell membrane integrity. The use of DWI enables the calculation of the apparent diffusion coefficient (ADC), which is a value that measures water diffusion in tissues. The quantitative analysis of ADC is easily performed on a scanner or a workstation. Movement of water is restricted movement in tumors, leading to a reduction in the ADC value [44, 45]. After the acquisition of DW images, an ADC map, which shows the ADC value of each voxel, can be correlated with T2-weighted images (Fig. 11).

DW scans are characterized by the b value (in s/mm^2), which is a function of diffusion gradient strength. For DWI, the diffusion sensitivity can be varied to control image contrast. DWI can be performed using multiple b field gradients. ADC maps are generated from DWI using a voxelwise calculation from the multiple DWI sequences. Therefore, prostate cancers display high signal on raw DWI because of restricted diffusion but low signal on ADC maps (Figs. 11B and 11C).

DW images can be acquired with various techniques. At our institution, DW images are obtained by applying a single-shot echo-planar imaging sequence with the same slice location as the T2 sequences (5000/75; parallel imaging factor, 2) Diffusion-encoding gradients are applied as bipolar pairs at b values of 0, 60, and 600 s/mm^2 along all three directions in the axial plane.

There is considerable debate regarding the most appropriate b values to use for DWI of the prostate. Recent studies have reported that the use of higher b values (1000–2000 s/mm^2) improves lesion detection [46–49].

Although an ADC value can be nonspecific because of its inherent variability (i.e., tissue diffusion can change based on the cellular microenvironment) [50], several studies show its usefulness in cancer detection in combination with T2-weighted images [48, 51–53]. Lim et al. [48] reported a sensitivity of 78–88% and specificity of 88–89% in prostate cancer detection by readers with various levels of experience, when an ADC map was combined with T2-weighted images as opposed to T2-weighted MR images alone (sensitivity, 67–74%; specificity, 77–79%).

Advantages of DWI include short acquisition time and ease of implementation. In addition, the use of parallel imaging with DWI can overcome some of its limitations of motion, susceptibility, and chemical-shift artifacts [44].

Dynamic Contrast-Enhanced MRI

In comparison with other functional MR sequences, experience with DCE-MRI is limited; however, interest in its application is growing. The principles of DCE-MRI are based on tumor angiogenesis. Tumors produce factors that promote vessel formation and increase permeability, compared with normal vessels [54, 55]. The enhancement pattern of cancerous tissue is different from that of normal tissue because there is also greater interstitial space in tumors and therefore a larger gap of contrast material concentration between the plasma and interstitial tissue. The values of contrast enhancement parameters such as mean transit time, blood flow, permeability of the surface area, and interstitial volume are significantly greater in cancerous tissue than in normal tissue [56–58]. Relative peak enhancement has been shown to be the most accurate perfusion parameter for pros-

tate cancer detection in the peripheral zone and central zone [59]. Kim et al. [60] reported that parametric imaging of the wash-in rate is more accurate for the detection of cancer in the peripheral zone than T2-weighted imaging alone. However, they also noted that the overlap between the wash-in rate for cancer and that for normal tissue in the transitional zone is significant.

There is currently no standard protocol for DCE-MRI of the prostate, but DCE-MRI of the prostate is usually performed using a fast imaging sequence. Three-dimensional gradient-echo sequences enable the entire prostate to be imaged in a few seconds. The DCE-MRI protocol used at our institution usually involves acquisition of unenhanced and multiphase contrast-enhanced images after the injection of gadopentetate dimeglumine (Magnevist, Bayer HealthCare) at a dose of 0.1 mmol/kg and a rate of 4 mL/s via a mechanical injector and applying a 3D fast gradient-echo sequence (field of view, 240 mm; matrix, 256 × 192; 3.9/1.8) yielding a fast temporal resolution (2.5–3.5 s).

Various perfusion parameters that allow localization of prostate cancer can be extracted from the dataset. Per-voxel evaluation of the enhancement-time course can be obtained qualitatively by characterizing kinetic enhancement curves. The integral under the dynamic curve is obtained for a targeted region of interest. Focal regions with large positive enhancement integral values are indicative of tumor involvement (Fig. 12). Furthermore, quantitative pharmacokinetic analysis of perfusion data can also be performed [61].

In conclusion, each of the various functional imaging methods discussed in this article has its advantages and limitations. The use of conventional MRI alone can have limited value in some patients. A combination of morphologic and functional techniques may enhance the clinical value of MRI in this setting (Fig. 13). However, it is important to understand that to perform and interpret high-quality functional imaging techniques, a dedicated team of treating physician, physicist, technician, and radiologist is vital. Functional imaging techniques show great promise for the diagnosis, staging, and treatment of prostate cancer.

References

1. Jemal A, Siegel R, Ward E, Hao Y, Xu J, Thun MJ. Cancer statistics, 2009. *CA Cancer J Clin* 2009; 59:225–249
2. Hricak H. MR imaging and MR spectroscopic imaging in the pre-treatment evaluation of prostate cancer. *Br J Radiol* 2005; 78[Spec No 2]:S103–S111
3. Gilligan T, Kantoff PW. Chemotherapy for prostate cancer. *Urology* 2002; 60:94–100
4. Thompson IM, Seay TM. Will current clinical trials answer the most important questions about prostate adenocarcinoma? *Oncology (Williston Park)* 1997; 11:1109–1117; discussion, 1118–1119, 1121
5. Coakley FV, Hricak H. Radiologic anatomy of the prostate gland: a clinical approach. *Radiol Clin North Am* 2000; 38:15–30
6. Hricak H, Dooms GC, McNeal JE, et al. MR imaging of the prostate gland: normal anatomy. *AJR* 1987; 148:51–58
7. KS, Kressel HY, Arger PH, Pollack HM. Age-related changes of the prostate: evaluation by MR imaging. *AJR* 1989; 152:77–81
8. Thompson IM, Pauler DK, Goodman PJ, et al. Prevalence of prostate cancer among men with a prostate-specific antigen level < or = 4.0 ng per milliliter. *N Engl J Med* 2004; 350:2239–2246
9. Thompson IM, Ankerst DP, Chi C, et al. Operating characteristics of prostate-specific antigen in men with an initial PSA level of 3.0 ng/ml or lower. *JAMA* 2005; 294:66–70
10. Gretzer MB, Partin AW. PSA markers in prostate cancer detection. *Urol Clin North Am* 2003; 30:677–686
11. Canto EI, Singh H, Shariat SF, et al. Effects of systematic 12-core biopsy on the performance of percent free prostate specific antigen for prostate cancer detection. *J Urol* 2004; 172:900–904
12. Singh H, Canto EI, Shariat SF, et al. Improved detection of clinically significant, curable prostate cancer with systematic 12-core biopsy. *J Urol* 2004; 171:1089–1092
13. Keetch DW, Catalona WJ, Smith DS. Serial prostatic biopsies in men with persistently elevated serum prostate specific antigen values. *J Urol* 1994; 151:1571–1574
14. Ellis WJ, Brawer MK. Repeat prostate needle biopsy: who needs it? *J Urol* 1995; 153:1496–1498
15. Roehrborn CG, Pickens GJ, Sanders JS. Diagnostic yield of repeated transrectal ultrasound-guided biopsies stratified by specific histopathologic diagnoses and prostate specific antigen levels. *Urology* 1996; 47:347–352
16. Presti JC Jr, Chang JJ, Bhargava V, Shinohara K. The optimal systematic prostate biopsy scheme should include 8 rather than 6 biopsies: results of a prospective clinical trial. *J Urol* 2000; 163:163–166
17. Makarov DV, Sanderson H, Partin AW, Epstein JI. Gleason score 7 prostate cancer on needle biopsy: is the prognostic difference in Gleason scores 4 + 3 and 3 + 4 independent of the number of involved cores? *J Urol* 2002; 167:2440–2442
18. Presti JC Jr. Prostate cancer: assessment of risk using digital rectal examination, tumor grade, prostate-specific antigen, and systematic biopsy. *Radiol Clin North Am* 2000; 38:49–58
19. Hittelman AB, Purohit RS, Kane CJ. Update of staging and risk assessment for prostate cancer patients. *Curr Opin Urol* 2004; 14:163–170
20. D'Amico AV, Renshaw AA, Cote K, et al. Impact of the percentage of positive prostate cores on prostate cancer-specific mortality for patients with low or favorable intermediate-risk disease. *J Clin Oncol* 2004; 22:3726–3732
21. Kamat AM, Jacobsohn KM, Troncoso P, Shen Y, Wen S, Babaian RJ. Validation of criteria used to predict extraprostatic cancer extension: a tool for use in selecting patients for nerve sparing radical prostatectomy. *J Urol* 2005; 174:1262–1265
22. Vira MA, Tomaszewski JE, Hwang WT, et al. Impact of the percentage of positive biopsy cores on the further stratification of primary grade 3 and grade 4 Gleason score 7 tumors in radical prostatectomy patients. *Urology* 2005; 66:1015–1019
23. Wang L, Mullerad M, Chen HN, et al. Prostate cancer: incremental value of endorectal MR imaging findings for prediction of extracapsular extension. *Radiology* 2004; 232:133–139
24. Wang L, Hricak H, Kattan MW, Chen HN, Scardino PT, Kuroiwa K. Prediction of organ-confined prostate cancer: incremental value of MR imaging and MR spectroscopic imaging to staging nomograms. *Radiology* 2006; 238:597–603
25. Wang L, Hricak H, Kattan MW, et al. Prediction of seminal vesicle invasion in prostate cancer: incremental value of adding endorectal MR imaging to the Kattan nomogram. *Radiology* 2007; 242:182–188
26. Jewett HJ. The present status of radical prostatectomy for stages A and B prostatic cancer. *Urol Clin North Am* 1975; 2:105–124
27. Hricak H, White S, Vigneron D, et al. Carcinoma of the prostate gland: MR imaging with pelvic phased-array coils versus integrated endorectal–pelvic phased-array coils. *Radiology* 1994; 193:703–709
28. Heijmink SW, Futterer JJ, Hambrock T, et al. Prostate cancer: body-array versus endorectal coil MR imaging at 3 T—comparison of image quality, localization, and staging performance. *Radiology* 2007; 244:184–195
29. Qayyum A, Coakley FV, Lu Y, et al. Organ-confined prostate cancer: effect of prior transrectal biopsy on endorectal MRI and MR spectroscopic imaging. *AJR* 2004; 183:1079–1083
30. Claus FG, Hricak H, Hattery RR. Pretreatment evaluation of prostate cancer: role of MR imaging and ^{1}H MR spectroscopy. *RadioGraphics* 2004; 24[suppl 1]:S167–S180

31. Brown TR, Kincaid BM, Ugurbil K. NMR chemical shift imaging in three dimensions. *Proc Natl Acad Sci U S A* 1982; 79:3523–3526
32. Kurhanewicz J, Vigneron DB, Hricak H, Narayan P, Carroll P, Nelson SJ. Three-dimensional H-1 MR spectroscopic imaging of the in situ human prostate with high (0.24-0.7-cm^3) spatial resolution. *Radiology* 1996; 198:795–805
33. Males RG, Vigneron DB, Star-Lack J, et al. Clinical application of BASING and spectral/spatial water and lipid suppression pulses for prostate cancer staging and localization by in vivo 3D ^{1}H magnetic resonance spectroscopic imaging. *Magn Reson Med* 2000; 43:17–22
34. Star-Lack J, Vigneron DB, Pauly J, Kurhanewicz J, Nelson SJ. Improved solvent suppression and increased spatial excitation bandwidths for three-dimensional PRESS CSI using phase-compensating spectral/spatial spin-echo pulses. *J Magn Reson Imaging* 1997; 7:745–757
35. Schricker AA, Pauly JM, Kurhanewicz J, Swanson MG, Vigneron DB. Dual-band spectral-spatial RF pulses for prostate MR spectroscopic imaging. *Magn Reson Med* 2001; 46:1079–1087
36. Star-Lack J, Nelson SJ, Kurhanewicz J, Huang LR, Vigneron DB. Improved water and lipid suppression for 3D PRESS CSI using RF band selective inversion with gradient dephasing (BASING). *Magn Reson Med* 1997; 38:311–321
37. Jung JA, Coakley FV, Vigneron DB, et al. Prostate depiction at endorectal MR spectroscopic imaging: investigation of a standardized evaluation system. *Radiology* 2004; 233:701–708
38. Zakian KL, Sircar K, Hricak H, et al. Correlation of proton MR spectroscopic imaging with Gleason score based on step-section pathologic analysis after radical prostatectomy. *Radiology* 2005; 234:804–814
39. Yu KK, Scheidler J, Hricak H, et al. Prostate cancer: prediction of extracapsular extension with endorectal MR imaging and three-dimensional proton MR spectroscopic imaging. *Radiology* 1999; 213:481–488
40. Joseph T, McKenna DA, Westphalen AC, et al. Pretreatment endorectal magnetic resonance imaging and magnetic resonance spectroscopic imaging features of prostate cancer as predictors of response to external beam radiotherapy. *Int J Radiat Oncol Biol Phys* 2009; 73:665–671
41. Coakley FV, Kurhanewicz J, Lu Y, et al. Prostate cancer tumor volume: measurement with endorectal MR and MR spectroscopic imaging. *Radiology* 2002; 223:91–97
42. Weinreb JC, Blume JD, Coakley FV, et al. Prostate cancer: sextant localization at MR imaging and MR spectroscopic imaging before prostatectomy—results of ACRIN prospective multi-institutional clinicopathologic study. *Radiology* 2009; 251:122–133
43. Le Bihan D, Breton E, Lallemand D, Grenier P, Cabanis E, Laval-Jeantet M. MR imaging of intravoxel incoherent motions: application to diffusion and perfusion in neurologic disorders. *Radiology* 1986; 161:401–407
44. Sato C, Naganawa S, Nakamura T, et al. Differentiation of noncancerous tissue and cancer lesions by apparent diffusion coefficient values in transition and peripheral zones of the prostate. *J Magn Reson Imaging* 2005; 21:258–262
45. Issa B. In vivo measurement of the apparent diffusion coefficient in normal and malignant prostatic tissues using echo-planar imaging. *J Magn Reson Imaging* 2002; 16:196–200s
46. Kim CK, Park BK, Lee HM, Kwon GY. Value of diffusion-weighted imaging for the prediction of prostate cancer location at 3T using a phased-array coil: preliminary results. *Invest Radiol* 2007; 42:842–847
47. Kitajima K, Kaji Y, Kuroda K, Sugimura K. High b-value diffusion-weighted imaging in normal and malignant peripheral zone tissue of the prostate: effect of signal-to-noise ratio. *Magn Reson Med Sci* 2008; 7:93–99
48. Lim HK, Kim JK, Kim KA, Cho KS. Prostate cancer: apparent diffusion coefficient map with T2-weighted images for detection—a multireader study. *Radiology* 2009; 250:145–151
49. Tamada T, Sone T, Toshimitsu S, et al. Age-related and zonal anatomical changes of apparent diffusion coefficient values in normal human prostatic tissues. *J Magn Reson Imaging* 2008; 27:552–556
50. Hosseinzadeh K, Schwarz SD. Endorectal diffusion-weighted imaging in prostate cancer to differentiate malignant and benign peripheral zone tissue. *J Magn Reson Imaging* 2004; 20:654–661
51. Yoshimitsu K, Kiyoshima K, Irie H, et al. Usefulness of apparent diffusion coefficient map in diagnosing prostate carcinoma: correlation with stepwise histopathology. *J Magn Reson Imaging* 2008; 27:132–139
52. Shimofusa R, Fujimoto H, Akamata H, et al. Diffusion-weighted imaging of prostate cancer. *J Comput Assist Tomogr* 2005; 29:149–153
53. Haider MA, van der Kwast TH, Tanguay J, et al. Combined T2-weighted and diffusion-weighted MRI for localization of prostate cancer. *AJR* 2007; 189:323–328
54. Brawer MK, Deering RE, Brown M, Preston SD, Bigler SA. Predictors of pathologic stage in prostatic carcinoma: the role of neovascularity. *Cancer* 1994; 73:678–687
55. Weidner N, Carroll PR, Flax J, Blumenfeld W, Folkman J. Tumor angiogenesis correlates with metastasis in invasive prostate carcinoma. *Am J Pathol* 1993; 143:401–409
56. Buckley DL, Roberts C, Parker GJ, Logue JP, Hutchinson CE. Prostate cancer: evaluation of vascular characteristics with dynamic contrast-enhanced T1-weighted MR imaging—initial experience. *Radiology* 2004; 233:709–715
57. Choi YJ, Kim JK, Kim N, Kim KW, Choi EK, Cho KS. Functional MR imaging of prostate cancer. *RadioGraphics* 2007; 27:63–75
58. Delorme S, Knopp MV. Non-invasive vascular imaging: assessing tumour vascularity. *Eur Radiol* 1998; 8:517–527
59. Engelbrecht MR, Huisman HJ, Laheij RJ, et al. Discrimination of prostate cancer from normal peripheral zone and central gland tissue by using dynamic contrast-enhanced MR imaging. *Radiology* 2003; 229:248–254
60. Kim JK, Hong SS, Choi YJ, et al. Wash-in rate on the basis of dynamic contrast-enhanced MRI: usefulness for prostate cancer detection and localization. *J Magn Reson Imaging* 2005; 22:639–646
61. Ocak I, Bernardo M, Metzger G, et al. Dynamic contrast-enhanced MRI of prostate cancer at 3 T: a study of pharmacokinetic parameters. *AJR* 2007; 189:849

FOR YOUR INFORMATION

The reader's attention is directed to the Self-Assessment Module for this article, which appears on the following pages.